IEEE Open Journal of
Antennas and Propagation

Received 22 September 2022; revised 4 November 2022; accepted 5 November 2022. Date of publication 9 November 2022;
date of current version 18 November 2022.

Digital Object Identifier 10.1109/OJAP.2022.3220851

A Compact, Band-Notched Ultra-Wideband Fully-Recessed Antenna With Pattern Diversity for V2X Communications

KE ZHANG[1] (Student Member, IEEE), ZHI HAO JIANG[1,2] (Member, IEEE), WEN LONG ZHOU[3], PENG PENG[3], AND WEI HONG[1,2] (Fellow, IEEE)

[1]School of Information Science and Engineering, Southeast University, Nanjing 210096, China

[2]Research Institute of Millimeter-Wave and Terahertz Technology (RIMMATT), Nanjing 211111, China

[3]Electrical and Electronic System Engineering, Ford Research & Engineering Center (China), Nanjing 210000, China

CORRESPONDING AUTHOR: ZHI HAO JIANG (e-mail: zhihao.jiang@seu.edu.cn)

This work was supported in part by the National Natural Science Foundation of China (NSFC) under Grant 62122019 and Grant 61801109; in part by the Scientific Research Foundation of Graduate School of Southeast University under Grant YBYP2115; in part by the Fundamental Research Funds for the Central Universities under Grant 2242021k30041; in part by the Ford Motor Incorporation; and in part by the High Level Innovation and Entrepreneurial Research Team Program in Jiangsu.

ABSTRACT In this paper, a compact, band-notched ultra-wideband (UWB) fully-recessed antenna with pattern diversity is proposed and demonstrated for vehicle-to-X communications. The antenna is composed of a multi-port central radiator fully embedded inside a bowl-shaped ground structure with a flush top. The multi-port central radiator consists of a top circular plate, four split-quarter conical monopoles, four vertically- and horizontally-orientated strips, a central metallic cylinder, and a bottom cylinder. Moreover, four F-shaped monopoles are loaded to the multi-port central radiator for producing two narrow notched bands. The integrated antenna achieves a form factor of $0.23\boldsymbol{\lambda}_{\mathbf{L}}^{\mathbf{3}}$, where $\boldsymbol{\lambda}_{\mathbf{L}}$ is the free space wavelength at the lowest working frequency. The proposed antenna was fabricated and characterized, achieving a measured $S_{11} < -10$ dB band ranging from 1.7 to 6 GHz with two stopbands at around 2.5 and 5.15 GHz for all four ports. Moreover, the measured mutual coupling is smaller than −15 dB, while the envelope correlation coefficients (ECCs) are below 0.1 between different input ports. A vertically-polarized (VP) omni-directional pattern can be supported when all four ports are excited simultaneously, whereas four directional patterns pointing towards different directions in the azimuthal plane can be realized when the four ports are excited individually. The demonstrated antenna is a promising candidate in multiple-input multiple-output communication systems for a wide variety of platforms.

INDEX TERMS Multiple-input multiple-output (MIMO) antennas, pattern diversity, recessed antenna, ultra-wideband (UWB), vehicular communications.

I. INTRODUCTION

IN VEHICULAR communication networks, the concept of vehicle-to-X (V2X) communication refers to the information exchange between a vehicle and other external communication nodes, *e.g.*, base stations, vehicles, pedestrians, infrastructures, and so on [1], [2]. In such a rapid-evolving network, three requirements are put forward for vehicle-mounted antennas to ensure a high signal quality. First, multiple services should be supported in the sub-6 GHz regime, *i.e.*, Long Term Evolution (LTE), Third-/Fourth-/FiFth-Generation (3G/ 4G/ 5G), Bluetooth, Wifi, and V2X (5905 – 5925 MHz). To this end, an ultra-wideband (UWB) antenna covering these frequency bands can significantly reduce the overall form factor of the device, as compared to using multiple antennas each with a different operational band [3], [4]. Secondly, a multiple-input multiple-output (MIMO) diversity antenna would be more desirable for simultaneously achieving a reliable link, a wide coverage, and/or a high channel capacity [5], [6]. As shown in Fig. 1 (a), if a vehicle needs to communicate with other

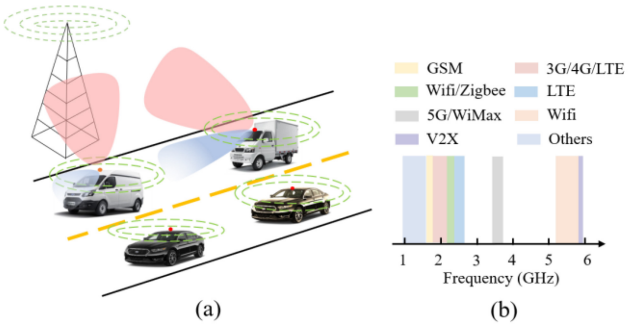

FIGURE 1. (a) 3-D concept map of the V2X communication network, (b) service bands in the sub-6 GHz regime.

nodes, *i.e.*, a particular base station or other ground terminals, a moderately-directive beam can be selected that radiates towards the targeted sector in both the azimuthal and elevation planes [7]. Moreover, in the azimuthal plane, omni-directional coverage is needed when communication links between vehicles are established [8], [9]. Thirdly, non-protruding flush-mounted antennas located beneath the vehicle roof would be more helpful to reduce aerodynamic drag as well as exhibit a better aesthetic rendering [10]. Consequently, a fully-recessed UWB antenna possessing pattern diversity would be a promising candidate for, but not limited to, vehicular communications.

Vertically-polarized (VP) antennas can provide a wide coverage for ground communications since the VP waves have lower path loss when they are propagating along the earth ground as compared to horizontally-polarized waves. On the other hand, omni-directional radiation can provide a wide coverage [11], [12]. Conventional single-port VP omni-directional antennas, such as narrow-band quarter-wave monopoles [13] and wideband metasurface-coated monopoles [14], [15], suffer from a high profile. Several planar antennas have been reported for achieving VP omni-directional radiation, including printed monopoles [16], [17], [18], slot loops [19], circular patches loaded with annular rings [20] or shorting pins [21], and metasurface-enabled radiators [22], [23], [24]. However, the bandwidths are narrow due to their high Q values. Recently, low-profile and wideband three-dimensional (3D) antennas have been proposed, such as a cone monopole antenna loaded with a grounded parasitic ring [25], meandered wires [26], a grounded cross-plate [27], and a capacitive-coupled patch [28], [29]. Although single-port antennas can provide broadband VP omni-directional patterns, they cannot support pattern diversity.

For multi-port VP omni-directional MIMO antennas, pattern diversities can be enabled by employing multiple radiating elements with different and orthogonal patterns. In [30], a wideband MIMO antenna, with a profile of $0.65\lambda_L$, was proposed, consisting of four VP F-shaped monopoles sequentially rotated by 90°. The antenna achieves a bandwidth of 105% by introducing parasitic stubs and a high port isolation by etching slots and adding metalized walls. In [31], a two-port VP MIMO antenna composed of a probe-fed cone monopole at the center and a ring radiator (consisting of four linear dipoles) around the cone was reported, exhibiting a bandwidth of 108% and a profile of $0.11\lambda_L$. A 4-channel MIMO antenna based on four probe-fed dielectric-loaded horns sharing a common top plate was proposed for achieving VP radiation within the sub-6 GHz bands [32]. By introducing shorting pins connecting the outer ring and ground plane, the antenna profile is reduced to $0.06\lambda_L$. On the basis of the transverse electromagnetic (TEM) horns [33], an eight-element circular array was also proposed to realize omni-directional radiation within a bandwidth of 153% [34]. However, the 3D-structures of these reported antennas all have a protruding part, which would cause unwanted aesthetic and/or electrical problems.

To address the protruding problem, the radiator can be designed to recess inside a concave ground structure. In [35], an eye-shaped monopole antenna partially recessed inside a shaped ground plane was described, achieving a bandwidth of 148% and a profile of $0.2\lambda_L$. However, the top part of the radiator still protrudes out from the plane of the ground. To further reduce the volume of the protruding part, several fully-recessed antennas have been proposed, including narrow-band designs, *e.g.*, patch and/or ring antenna [36], and slot antenna [37], as well as wideband designs, *e.g.*, cone monopolar antennas [38], Vivaldi antenna [39], and TEM horn [40]. In [41], a material-based design approach of embedded-monopole was reported theoretically based on transformation optics, with a two-dimensional (2D) demonstrating prototype realized by negative-index metamaterials operating over a narrow frequency range [42]. Therefore, antenna designs that have fully-recessed radiators without any protruding parts are highly desirable in vehicular communications, particularly for roof-mount communication modules, which, however, have not been achieved yet.

In this paper, the design and experiments of a compact four-port band-notched UWB fully-recessed antenna with pattern diversities is reported. The proposed antenna is composed of a multi-port central radiator fully recessed inside a bowl-shaped ground structure, covering a broad frequency range from 1.7 to 6 GHz. In addition, F-shaped monopoles are loaded to generate two notched stopbands at 2.4 and 5.2 GHz for inter-system interference suppression. The antenna can support omni-directional patterns when all four ports are excited simultaneously, and four directional patterns pointing towards different directions when the four ports are excited individually. The paper is organized as follows. In Section II, the antenna configuration and design procedure are presented. The impacts and optimization of the key design parameters are described in Section III. Section II shows the simulated and measured performance of the UWB diversity antenna with dual notched bands. Finally, concluding remarks are drawn in Section VI.

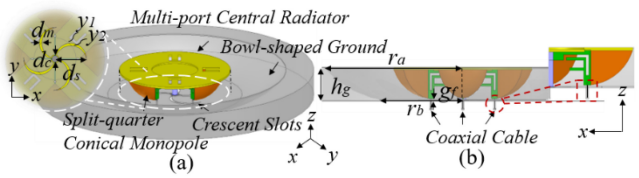

FIGURE 2. (a) Front and (b) side views of the proposed antenna. The geometrical dimensions are $r_a = 120$, $r_b = 72.3$, $h_g = 29$, $g_f = 1$, $d_s = 38$, $d_m = 3$, $d_c = 10$, all in millimeters.

II. ANTENNA DESIGN

A. ANTENNA STRUCTURE

As depicted in Fig. 2, the configuration of the proposed fully-recessed antenna includes two metallic parts – a multi-port central radiator and a bowl-shaped ground structure, where the former one is fully embedded at the center of the latter one. The two parts have a flush top such that no structure is protruding out. The multi-port central radiator, as shown in Fig. 3, is composed of a top circular plate, four split-quarter conical monopoles, four horizontally-orientated strips, four vertically- orientated strips, a central metallic cylinder, and a bottom cylinder. Among them, the radius and thickness of the top circular plate are r_1 and h_1, respectively, wherein a sunken circular cylinder with a radius of r_2 and a height of h_2 is located at the center. On the top circular plate, four U-shaped slots are cut along the mirror-symmetry lines between adjacent split-quarter conical monopoles with side lengths of l_{u1} and l_{u2}, and a width of w_{u1}. Underneath the top circular plate, four split-quarter conical monopoles are distributed symmetrically around the center, each with a flare angle of φ_f and a radius of l_m. Their curved generatrices follow the exponential function: $z = 0.316 \times e^{0.074y} - 10.58 \times e^{-0.0816y}$, with the value of y varying from 30 to 60 mm. In addition, four horizontally-orientated strips ($l_1 \times w_1$) and vertically-orientated strips ($l_2 \times w_2$) are attached to the top circular plate and four split-quarter conical monopoles, respectively. In the vertically- and horizontally-oriented strips, the inverted L-shaped slots with lengths of ($l_{f1} + l_{f3}$) are cut and parasitic strips with lengths of l_{f2} are loaded to form F-shaped monopoles for producing two resonances. Moreover, a central metallic cylinder with a height of l_3 and a dimeter of d_3 is loaded at the center and a bottom cylinder with a diameter of d_p is used as the pedestal of the multi-port central radiator, which are used for improving port isolation. Four 50 Ω coaxial probes, each with a distance of d_f away from the center, are connected to the four split-quarter conical monopoles at the bottom through small circular holes etched out on the bowl-shaped ground structure. It should be noted that a gap with a height of g_f existing between the feeding position and bottom of the ground plane directly relates to the working bandwidth of the antenna.

For the ground plane, a bowl-shaped metallic structure is formed by cutting a cone out of a metallic cylinder with a height of h_g and a radius of 150 mm. The top and bottom radii of the bowl-shaped ground are r_a and r_b, while the

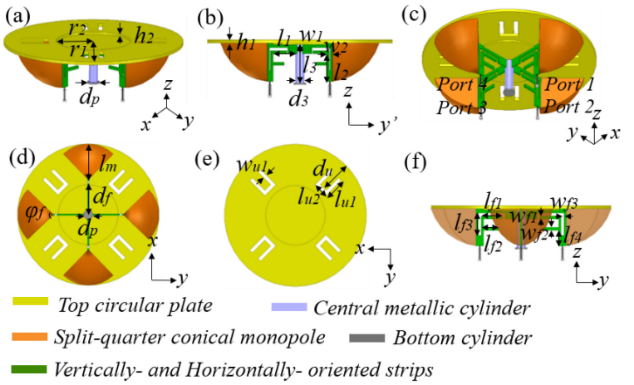

FIGURE 3. (a) Front, (b) side, (c) rear, (d) bottom, (e) top, and (f) side views of the multi-port central radiator. The geometrical dimensions are $r_1 = 60$, $r_2 = 25.4$, $h_1 = 2$, $h_2 = 1.5$, $l_1 = 22$, $w_1 = 7$, $l_2 = 18$, $w_2 = 5.1$, $l_3 = 26$, $d_3 = 6$, $l_m = 30$, $d_p = 8$, $d_f = 27.52$, $d_u = 27$, $l_{u1} = 18$, $w_{u1} = 3$, $l_{u2} = 13$, $l_{f1} = 14$, $w_{f1} = 2$, $l_{f2} = 10$, $w_{f2} = 2$, $l_{f3} = 15$, $w_{f3} = 2$, $l_{f4} = 10.5$, all in millimeters, $\varphi_f = 90°$, and $\hat{y}' = (\hat{x}+\hat{y})/\sqrt{2}$.

curved generatrix follows the exponential function of $z = 39.18 \times exp(-(y - 142.9)^2/38.32^2)$, with the value of y varying from 72.3 to 120 mm. As it can be seen from Fig. 2(a), on the bottom of the bowl-shaped ground, four crescent slots, with a largest width of d_m, and a central cylindrical aperture with a diameter of d_c were cut out for improving the isolation between all the input ports. The crescent shape was chosen for the slots since it can elongate the current path within a compact area, thereby improving the mutual coupling induced by direct current flow between ports. The outer and inner lines of the crescent slots, i.e., $y1$ and $y2$, follow the circular functions of $y1 = \sqrt{ds^2/4 - (x - ds/2)^2}$, and $y2 = d_m + \sqrt{ds^2/4 - (x - ds/2)^2}$, with the values of x both varying from 0 to 38 mm. The high frequency structure simulator (HFSS) was used for numerically evaluating the properties of the antenna.

B. DESIGN PROCEDURE

In this section, the design procedure of the proposed antenna structure is exhibited, evolving gradually from a simple vertically-orientated monopole to the final design. The inset in Fig. 4, *i.e.,* ANT I, shows that the proposed antenna starts with a pin-fed monopole with $h_{v1} = 34$ mm placed on a finite ground plane with $R_{gnd} = 150$ mm. The simulated S_{11} curve exhibits a single resonance at around 2 GHz with a −10 dB impedance bandwidth of about 290 MHz, when the length of the pin-fed monopole is about a quarter wavelength (see ANT I). An additional resonance can be identified at 6.3 GHz due to the occurrence of the first higher-order resonant mode. In order to broaden the operational bandwidth, the thin monopole was re-shaped into a modified cone, named as ANT II. The top diameter d_{v2} and height h_{v2} of the modified conical monopole are 32 and 27 mm, respectively. The smooth generatrix follows the function of $z = 0.78 \times e^{0.21y}$, with $y \in [0.5,\ 16]$. It can be seen from Fig. 4 that the impedance bandwidth of ANT II is broadened significantly, possessing a simulated $S_{11} < -10$ dB band ranging from 1.92 to

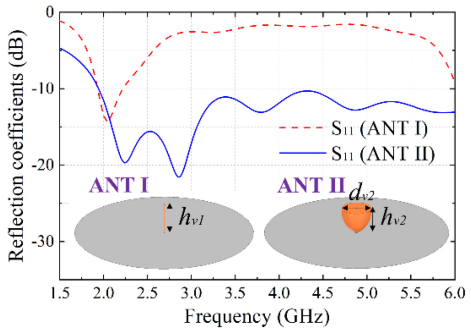

FIGURE 4. Simulated reflection coefficients of ANT I and ANT II. The geometrical dimensions are: $h_{v1} = 34$, $h_{v2} = 27$, $d_{v2} = 32$, all in millimeters. The insets show the configurations of ANT I and ANT II.

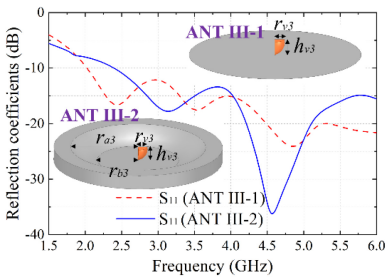

FIGURE 5. Simulated reflection coefficients of ANT III-1 and ANT III-2. The geometrical dimensions are: $r_{v3} = 16$, $h_{v3} = 27$, $r_{a3} = 104$, $r_{b3} = 72.7$, all in millimeters. The insets show the configurations of ANT III-1 and ANT III-2.

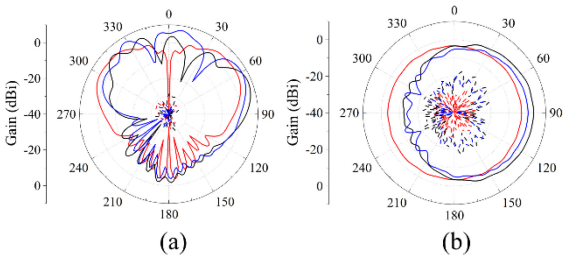

FIGURE 6. Simulated gain patterns of ANT II (Red line), ANT III-1 (Black line), and ANT III-2 (Blue line) at 5.9 GHz in the (a) *yz*- and (b) *xy*-planes. Solid line (——): E_θ; Dash line (——): E_φ.

6 GHz, because the curved genetrix contributes to the identical characteristic impedance along all the points so as to produce wideband performance. Meanwhile, the variation hardly makes a difference on the radiation patterns between ANT I and ANT II (not shown here), both exhibiting omni-directional conical-shaped patterns within their $S_{11} < -10$ dB frequency bands.

For enhancing the channel capacity without consuming more spectrum resources, MIMO antennas that utilize spatial, pattern and/or polarization diversities have been widely employed [43], [44], which inevitably requires a compact form factor. If ANT II is used as a single element of a MIMO array of four elements that are arranged into a circular array, the overall array would appear bulky with poor isolation. Therefore, ANT II is split into four parts, each containing a quarter of the modified conical monopole (see ANT III-1), which is referred to as the split-quarter conical monopole.

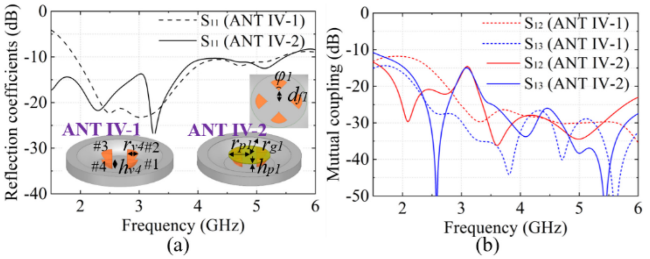

FIGURE 7. Simulated (a) reflection coefficients and (b) mutual coupling of ANT IV-1 and ANT IV-2. The geometrical dimensions are: $r_{v4} = 30.48$, $h_{v4} = 25$, $r_{p1} = 60$, $r_{g1} = 120$, $h_{p1} = 2$, $d_{f1} = 29.52$, all in millimeters, and $\varphi_1 = 90$ deg. The insets show the configurations of ANT IV-1 and ANT IV-2.

In this configuration, the radius, height, and generatrix of ANT III-1 are the same as those of ANT II. It can be seen that the $S_{11} < -10$ dB bandwidth of ANT III-1 is nearly the same as that of ANT II, indicating that the splitting action has no influence on the UWB characteristics of the radiator. However, the radiation pattern of ANT III-1 in the *xy*-plane becomes more directive as compared to that of ANT II. Moreover, in the *yz*-plane, a larger gain is obtained within the angular range of $60° \leq \theta \leq 90°$ [see Fig. 6].

On the other hand, a number of platforms require VP non-protruding antennas that are fully embedded below the horizon of the platform roof. To this end, the flat ground is modified into a bowl-shaped ground such that the split-quarter conical monopole at the center becomes a recessed radiator (see the inset of Fig. 5 for ANT III-2). The top and bottom radii of the bowl-shaped ground are r_{a3} and r_{b3}, respectively. It should be noted that the inner generatrices of the bowl-shaped ground structures are kept the same throughout the paper. The inner wall of the bowl-shaped ground functions partially as a reflector especially at low frequencies, which would affect the impedance matching of the antenna, causing a resonant frequency blueshift. As shown in Fig. 6, the loading of the bowl-shaped ground only has a minor influence on the radiation patterns in the *yz*- and *xy*-planes, demonstrating that the fully-recessed topology would not significantly change the radiation characteristics [41], [42].

Pattern diversities can be achieved by using a multiport multimode antenna that radiate different and orthogonal patterns, which can enable a reliable link and/or a higher channel capacity. Here, four ANT III-2 elements are distributed annularly with a sequential rotation of 90° that constitute a MIMO antenna array (see ANT IV-1 in Fig. 7(a)), implying that an omni-directional coverage could be supported when all the elements are excited in phase. In this process, the four elements are moved outward away from the center by d_{f1}, similar to an exploded modified conical monopole each with a flare angle of φ_1. As shown in Fig. 7, the simulated S_{11} curves indicate that the -10 dB impedance bandwidth of ANT IV-1 ranges from 1.9 to 5.4 GHz, with an impedance match worse than that of ANT III-2 at higher frequencies. This is because the distance between the split-quarter conical monopole and curved inner wall of the bowl-shaped

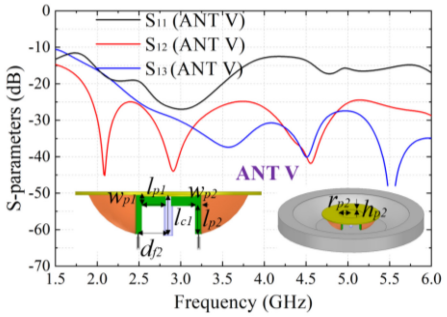

FIGURE 8. Simulated S-parameters of ANT V. The geometrical dimensions are: l_{p1} = 22, w_{p1} = 7, l_{p2} = 18, w_{p2} = 5.1, l_{c1} = 25, d_{f2} = 27.52, r_{p2} = 25.4, h_{p2} = 2, all in millimeters. The inset shows the configuration of ANT V.

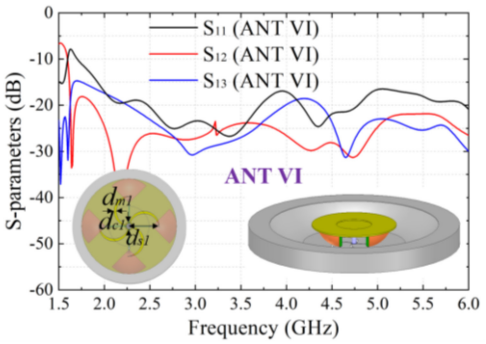

FIGURE 9. Simulated S-parameters of ANT VI. The geometrical dimensions are: d_{m1} = 3, d_{s1} = 38, d_{c1} = 10, all in millimeters. The inset shows the configuration of ANT VI.

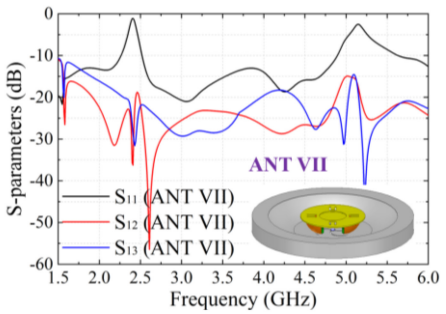

FIGURE 10. Simulated S-parameters of ANT VII. The inset shows the configuration of ANT VII.

ground becomes smaller, yielding an increased capacitance in the input impedance of the radiator at frequencies from 4 to 6 GHz. To enable a better integration and extend the low frequency end of the operational band, a metallic circular plate with a radius of r_{p1} and a thickness of h_{p1} is loaded on the top of the four elements. When each element is excited, the other three can be considered as parasitic loadings that lengthen the current path, thereby inducing extra resonances at frequencies below 2 GHz and broadening the bandwidth [see Fig. 7(a)]. Moreover, comparing to ANT IV-1, the mutual coupling between adjacent ports of ANT IV-2, *i.e.*, S_{12}, is reduced from −11.7 to −15.6 dB, while the mutual coupling between opposite ports, *i.e.*, S_{13}, is increased slightly from −14.3 to −12.1 dB, which could be improved by other de-coupling techniques [see Fig. 7(b)]. At the same time, there is almost no difference between ANT IV-1 and ANT IV-2 in terms of the radiation patterns.

To ensure a mechanical robustness between the multi-port central radiator and bowl-shaped ground, a central cylinder is added at the center of the ground to support the multi-port central radiator. Moreover, four vertically- and horizontally-orientated strips connecting to the inner edges of the four split-quarter conical monopoles are introduced for impedance matching at higher frequencies. As shown in Fig. 8, the S_{11} of ANT V is smaller than −10 dB from 1.5 to 6 GHz, exhibiting a much broader impedance bandwidth than that of ANT IV-2. It should be noted that the improved impedance match at high frequencies is primarily attributed to the vertically- and horizontally-orientated strips, bringing inductive effects for promoting the impedance matching. The mutual coupling between adjacent ports, *i.e.*, S_{12}, is smaller than −15 dB within the entire operational band, whereas the port isolation between the opposite ports, *i.e.*, S_{13}, reaches 12.7 dB at 1.7 GHz. This increased mutual coupling at 1.7 GHz mainly results from the surface currents directly flowing between ports. In contrast, the mutual coupling at 3.1 GHz is drastically reduced from −15 dB of ANT IV-2 to −31 dB of ANT V, which is due to the existence of the central metallic cylinder that suppresses direct spatial-wave coupling between adjacent and opposite ports.

To further improve the port isolation between adjacent and opposite ports, a slot-cutting technique for blocking the direct current paths is used. On the bottom of the bowl-shaped ground, four counter-clockwise crescent-shaped slots and a central circular hole with a diameter of d_{c1} are cut out [see Fig. 2]. It can be seen from Fig. 9 that while the S_{11} of ANT VI are all smaller than −10 dB within the band of interest, *i.e.*, 1.7 – 6 GHz, the mutual coupling between adjacent and opposite ports are reduced from −15 to −18.1 dB and from −12.7 to −14.7 dB, respectively. It should be noted that the presence of the crescent slots would cause slight increasement of the back radiation towards the lower half-space with a maximum level of no more than −10 dB.

Since WLAN communication bands (2.4 /5.2 GHz) are widely used for in-vehicle entertaining systems, it would be beneficial for vehicle-mounted antennas to have narrow notched-bands to physically suppress crosstalk between in-car and out-of-car communications. By integrating resonant structures into the antenna, two narrow notched bands at 2.4 and 5.2 GHz can be achieved. In general, the notched bands can be realized by etching slots in the patch [45], [46] and loading additional resonators around the planar monopole [47], [48]. As shown in Fig. 10, ANT VII is obtained by loading four F-shaped monopoles on the vertically-orientated strips and four U-shaped slots on the top circular plate of ANT VI. First, the four inverted L-shaped slots in the vertically- and horizontally-strips, where the strong currents occur, are cut to form the longer-length arms of the F-shaped monopole with an electrical length (l_{f1} +

TABLE 1. Comparison of the fully-recessed antennas.

Ref.	Frequency (GHz)	Bandwidth	Diversity	Gain (dBi(c))	Notched band
[10]	1.65	103%	No	>2.5	No
[38]	0.32	76%	No	>3	No
[39]	13	77%	No	>8	No
[40]	4.5	111%	No	>5	No
[36]	1.18 / 1.58 / 2.34	7.2% / 3.4% / 10.6%	Yes	5 / 5 / 7	No
[37]	1.472 / 2.339	2.7% / 0.5%	Yes	>2 / >2	No
[49]	2.2	47%	Yes	>6	No
This work	3.85	112%	Yes	>6	Yes

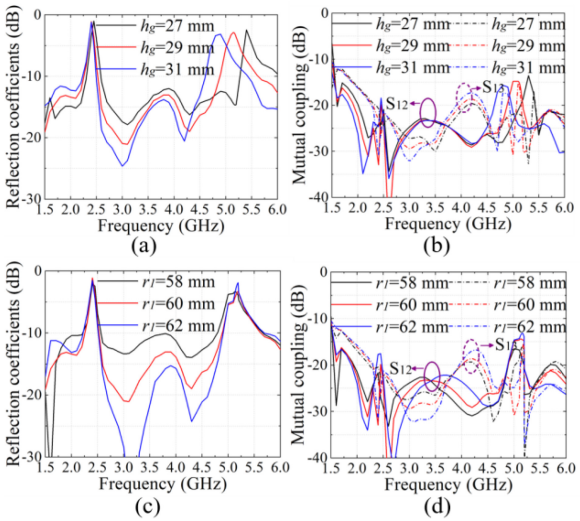

FIGURE 11. Parametric studies on (a) reflection coefficients and (b) mutual coupling by varying h_g; (c) reflection coefficients and (d) mutual coupling by varying r_1.

l_2) of a quarter wavelength at 2.4 GHz. Secondly, four parasitic strips with a length of l_{f2} are loaded to constitute the shorter-length arms of the F-shaped monopole resonating at 5.2 GHz with a length of ($l_{f2} + l_{f4}$). Moreover, four U-shaped slots are cut from the top circular plate to improve the impedance matching at 5.9 GHz, which is affected by the added stopband structure resonating at 5.2 GHz.

It should be mentioned that the antenna not only can be fully recessed inside a ground structure, but it also has two notched bands for avoiding the undesired crosstalk between in-car and out-of-car systems, differentiating it from the previously reported antennas [32], [34]. Table 1 gives the performance comparison among the proposed and previously-reported fully-recessed antennas. Compared with other fully-recessed antennas, the antenna can achieve a wider working bandwidth and diversity performance within the entire operational band.

III. PARAMETRIC STUDIES

In this section, the impacts of the profile, radius of the top circular plate, and lengths of two arms of the F-shaped monopole on the working bandwidth and mutual coupling of the antenna will be discussed.

First, antennas with a low profile are always desirable for various platforms, such as vehicles, for electrical as well as aesthetic considerations. In the premise of no protruding part, the integrated antenna profile, *i.e.*, h_g, should be optimized. It can be seen from Fig. 11(a) and (b) that, when the value of h_g increases, the notched band at 5.2 GHz would shift towards low frequencies, due to the elongated electrical length of the longer-length arm caused by the increased profile, while the notched band at 2.4 GHz remains almost unchanged. Since the shifting of the stopband at 5.2 GHz would also affect the input impedance at the 5.9 GHz V2X band, as a balance of impedance matching and mutual coupling, h_g is chosen to be 29 mm.

Secondly, the radius of the top circular plate, *i.e.*, r_1, primarily determines the miniaturization degree of the multi-port central radiator. As shown in Fig. 11(c) and (d), by varying r_1 from 58 to 62 mm, the impedance match becomes better in the band from 2.5 to 5 GHz, while it shows an opposite trend at frequencies around 5.9 GHz. Moreover, for achieving an S_{11} of smaller than -13 dB within the low band of interest at frequencies around 1.7 and 1.9 GHz, $r_1 = 60$ mm was selected. Meanwhile, the mutual coupling is almost unaffected by r_1, where S_{12} and S_{13} are smaller than -13.5 and -12.5 dB for all three values of r_1, respectively.

Thirdly, resonances at 2.4 and 5.2 GHz are excited by loading two quarter-wavelength monopole structures for generating two stopbands, respectively. Thus, the locations of the notched bands are determined by the length of the two arms of the F-shaped monopoles, *i.e.*, l_{f1} and l_{f2}. As shown in Fig. 12(a) and (b), by increasing l_{f1}, the notched band at 2.4 GHz with a peak S_{11} value of about -2 dB experiences a redshift, while the S_{11} magnitude at 5.2 GHz is only slightly affected. The mutual coupling between ports, *i.e.*, S_{12} and S_{13}, remain almost unchanged. For the notched band at 5.2 GHz, when l_{f2} increases, the resonance undergoes a redshift towards lower frequencies [see Fig. 12(c) and (d)]. Similarly, the change of l_{f2} has almost no influence on the properties of the low-frequency stopband and port isolation. After optimization, l_{f1} and l_{f2} are chosen to be 16 and 10 mm, respectively.

IV. SIMULATED AND EXPERIMENTAL RESULTS

A. S-PARAMETERS AND RADIATION PATTERNS

To validate the performance of the integrated fully-recessed band-notched UWB diversity antenna, the multi-port central radiator and bowl-shaped ground were fabricated separately using a high-precision cutting machine and assembled into an integrated fully-recessed antenna structure [see Fig. 13(a)-(c)]. Four mini-coaxial cables, which are directly soldered to the bottom of the vertically-orientated strips, are used for feeding the multi-port central radiator (not shown here). Fig. 13(d) shows a photograph of the fully-recessed band-notched UWB diversity antenna mounted on the car roof.

The *S*-parameters of the antenna were characterized by a vector network analyzer. During the measurement, when

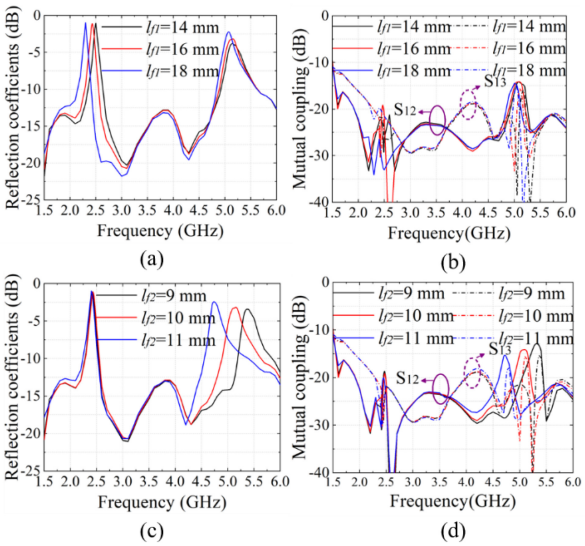

FIGURE 12. Parametric studies on (a) reflection coefficients and (b) mutual coupling by varying l_{f1}; (c) reflection coefficients and (d) mutual coupling by varying l_{f2}.

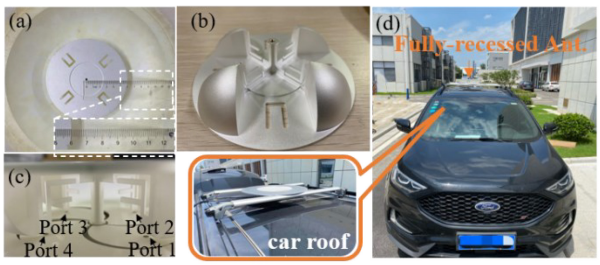

FIGURE 13. (a) Exploded, (b) top, and (c) side views of the antenna prototype (ANT VII); (d) A photograph of the antenna prototype mounted on the car roof.

two of the four ports were excited, the remaining ports were terminated by 50 Ω matched loads. Fig. 14 depicts the measured reflection coefficients of all four input ports, as well as the mutual coupling between adjacent and opposite ports, showing a good agreement between the simulated and measured results. For Port 1, the measured $S_{11} < -10$ dB band ranges from 1.7 to 6 GHz, with two narrow bands spanning from 2.4 to 2.64 GHz and from 4.98 to 5.6 GHz. The peak S_{11} values in the two narrow stopbands for all four ports are around −2.8 and −3 dB at 2.5 and 5.15 GHz, respectively. The measured mutual coupling between adjacent and opposite ports, *i.e.*, S_{12} and S_{13}, are smaller than -15 dB throughout the entire band.

The radiation patterns and gain values of the integrated fully-recessed band-notched UWB diversity antenna prototype were measured in a spherical near-field anechoic chamber. It also should be noted that when one port is excited, the other three ports should be terminated by 50 Ω matched loads. Fig. 15 reports the normalized radiation patterns at 1.7, 1.9, 3.5, and 5.9 GHz in the *xz*-, *yz*-, and *xy*-planes when Port 1 is excited, exhibiting a good correspondence between the simulated and measured results. In the *yz*-plane, the patterns indeed show that majority of the power is radiated towards the upper region of +*z*-direction

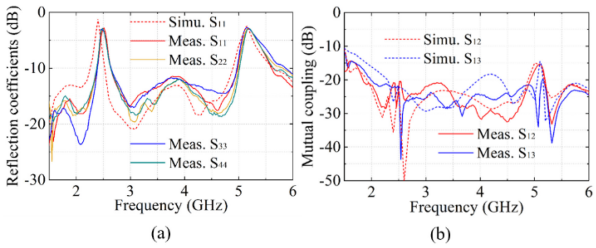

FIGURE 14. Simulated and measured (a) reflection coefficients and (b) mutual coupling of ANT VII.

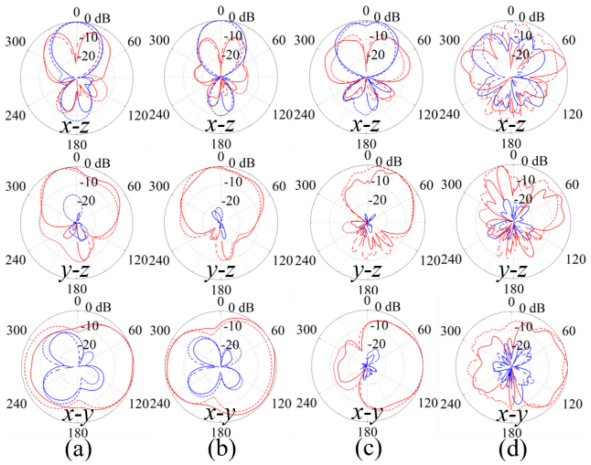

FIGURE 15. Simulated and measured normalized radiation patterns of ANT VII when Port 1 is excited at (a)1.7, (b) 1.9, (c) 3.5, and (d) 5.9 GHz. Red solid line (——): measured E_θ, blue solid line (——): measured E_φ, Red dashed line (– – –): simulated E_θ, blue dashed line (– – –): simulated E_φ.

with a cross-polarization level of smaller than −26 dB and a maximum level of less than −10 dB towards the lower half-space for all frequencies. At first, the main beams radiate towards the directions in between +*z*- and -*y*-directions at 1.7 GHz. As frequency increases to 5.9 GHz, the main beam shifts towards +*y*-direction gradually. Moreover, in the *xy*-plane, when Port 1 is excited, the main beams point to the +*y* direction with a cross-polarization level of smaller than −20 dB. When four ports are excited in phase simultaneously, the beams corresponding to four input ports merge into omni-directional patterns. In the measurement, for communications with the base station, quasi-omni-directional patterns are achieved in the horizontal planes with different elevation angles, *i.e.*, $\theta = 60°$, 70°, 80°, and 90° [see Fig. 16]. The gain deviations are smaller than 3, 3, 2, and 4.7 dB at 1.7, 1.9, 3.5, and 5.9 GHz, while the realized gain levels are higher than −5 dBi in between $\theta = 60°$ and $\theta = 90°$ for all frequencies. It also should be noted that the antenna placed on the Teflon pedestal is not perfectly perpendicular to the ground plane during the assembly process, which would slightly affect the impedance matching and pattern symmetry.

For a better illustration of the operating principle of the antenna, the current distributions on the proposed fully-recessed antenna due to Port 1 excitation at 1.7, 1.9, 3.5, and 5.9 GHz are displayed in Fig. 17. At low frequencies of 1.7

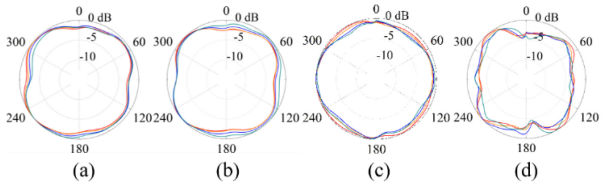

FIGURE 16. Measured normalized radiation patterns of ANT VII in the *xy*-plane when four ports are excited in phase at (a) 1.7, (b) 1.9, (c) 3.5, and (d) 5.9 GHz. Red solid line: measured E_{total} at $\theta = 60°$; Origin solid line: measured E_{total} at $\theta = 70°$; Blue solid line: measured E_{total} at $\theta = 80°$; Green solid line: measured E_{total} at $\theta = 90°$.

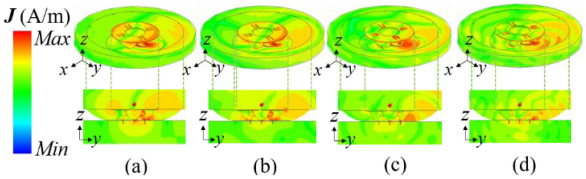

FIGURE 17. Snapshots of the simulated surface current distributions of ANT VII at (a) 1.7, (b) 1.9, (c) 3.5, and (d) 5.9 GHz.

and 1.9 GHz, the current propagates along the *y*-direction on the top circular plate, generating broadside patterns in the *yz*-plane [see Fig. 17(a) and (b)]. Particularly, at 1.9 GHz in the *yz*-plane, slot radiation between the rim of the top circular plate and top edge of the ground structure can be identified, resembling a half-wavelength resonant mode. Moreover, the currents between the top circular plate and bowl-shaped ground radiate towards $+z$-directions, indicating that the inner wall of the bowl-shaped ground functions as a metallic reflector. At 3.5 and 5.9 GHz, stronger currents can be found on the split-quarter conical monopole rather than the top circular plate, which implies that the radiation is mainly attributed to the travelling wave propagating in between the curved ground plane and split-quarter conical monopole [see Fig. 17(c) and (d)].

In order to understand the stopband generation of ANT VII, the surface current distributions at 2.4 and 5.2 GHz are displayed in Fig. 18. It can be seen that strong currents are concentrated along the longer-length arm of the F-shaped monopole, which has a length of about a quarter wavelength at 2.4 GHz. Meanwhile, as revealed by the weak currents on the top circular plate, the U-shaped slots make little influence on the low frequency stopband. The second stopband centered at 5.2 GHz is generated by the shorter-length arm of the F-shaped monopoles on which the fields are concentrated [see Fig. 18(b)]. At 5.9 GHz, strong fields can be found around the U-shaped slots, implying that the introduced capacitive effects indeed help improving the impedance matching (not shown here).

Fig. 19 depicts the measured peak realized gains of ANT VII versus the frequency when the four ports are excited individually, which shows that the measured results agree well with the simulated results. Apart from the two narrow frequency bands near 2.5 and 5.15 GHz, the gain varies between 6 and 9.5 dBi in the majority of the bands. At

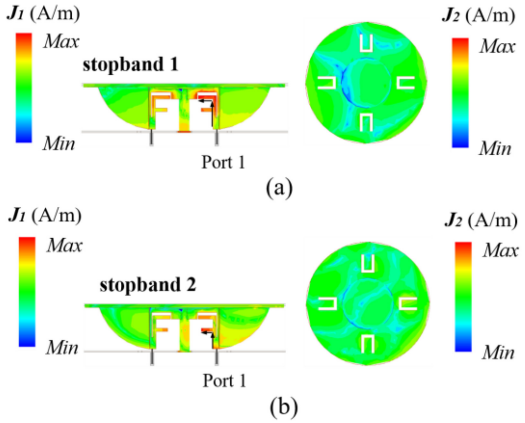

FIGURE 18. Simulated surface current distributions of the multi-port central radiator in ANT VII when Port 1 is active at (a) 2.4 and (b) 5.2 GHz.

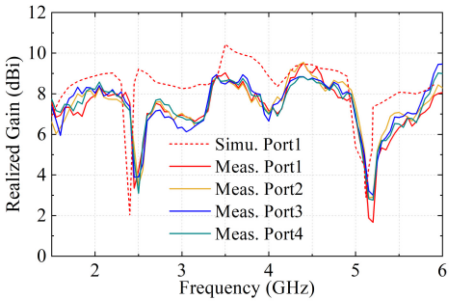

FIGURE 19. Simulated and measured realized gain of ANT VII for four ports.

2.5 GHz, the realized gain is about 3 dBi, whereas the realized gain is about 2 dBi at 5.15 GHz. The discrepancy can be attributed to fabrication tolerance and the assembling errors.

B. DIVERSITY PERFORMANCE

The envelope correlation coefficient (ECC) was calculated for validating the diversity performance of the antenna, which can be expressed based on the radiation patterns of the antenna in an isotropic propagation environment as [50], [51]

$$\rho_e = \frac{\left|\iint_{4\pi}\left[F_{Porti}(\theta,\varphi)*F_{Portj}(\theta,\varphi)\right]d\Omega\right|^2}{\iint_{4\pi}\left|F_{Porti}(\theta,\varphi)\right|^2 d\Omega \iint_{4\pi}\left|F_{Portj}(\theta,\varphi)\right|^2 d\Omega}, \quad (1)$$

where $F_{Porti(j)}(i = 1, \text{and } j = 2, 3)$ represents the complex 3D far-field pattern for Ports *i, j*, and the symbol "$*$" denotes the Hermitian product. The second alternative method for ECC calculation is based on the scattering parameters, which can be expressed as [52]

$$\rho_e = \frac{\left|S_{ii}^* S_{ij} + S_{ji}^* S_{jj}\right|^2}{\left(1-\left|S_{ii}\right|^2-\left|S_{ji}\right|^2\right)\left(1-\left|S_{jj}\right|^2-\left|S_{ij}\right|^2\right)}, \quad (2)$$

where $S_{i(j),i(j)}$, $(i \neq j \text{ and } i, j = 1, 2, 3)$ represents the complex *S*-parameters for Port *i* and/or Port *j*.

Fig. 20 shows the ECC curves calculated by the simulated and measured complex 3D radiation patterns and scattering parameters for adjacent and opposite ports, *i.e.*, Ports

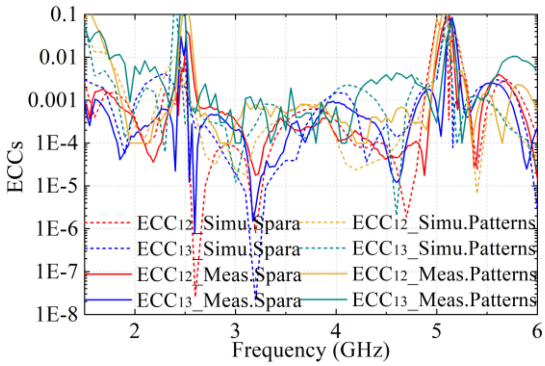

FIGURE 20. Simulated and measured ECCs of ANT VII for adjacent and opposite ports.

1, 2, and 3. It can be seen that the ECC values calculated by the simulated and measured radiation patterns and scattering parameters agree well with each other within the entire band, which are all below 0.05 from 1.7 to 6 GHz, except for frequencies near the two stopbands around 2.5 and 5.15 GHz. In short, the simulated and measured results demonstrate its low correlation for ensuring good channel characteristics.

V. CONCLUSION

In summary, a compact, band-notched UWB fully-recessed antenna with pattern diversities is proposed and demonstrated for V2X communications. The antenna is composed of a multiport central radiator fully embedded at the center of a bowl-shaped ground structure. The notched bands are achieved by incorporating four F-shaped monopoles that produce two resonances at 2.4 and 5.2 GHz. The mutual coupling reduction is realized by cutting crescent slots on the bottom of the bowl-shaped ground. The proposed antenna is fabricated and characterized, achieving an $S_{11} < 10$ dB band from 1.7 to 6 GHz with two notched bands centered at 2.5 and 5.15 GHz for all four ports, a mutual coupling of less than -15 dB, and an ECC below 0.1. The antennas provide omni-directional patterns when all four ports are excited in phase, and four directional beams when the four ports are excited individually. The demonstrated fully-recessed diversity antennas are promising candidates for MIMO multiservice devices in vehicles and other no protruding platforms.

REFERENCES

[1] K. Abboud, H. A. Omar, and W. Zhuang, "Interworking of DSRC and cellular network technologies for V2X communications: A survey," *IEEE Trans. Veh. Technol.*, vol. 65, no. 12, pp. 9457–9470, Dec. 2016.

[2] B. D. Shang, L. J. Liu, J. C. Ma, and P. Z. Fan, "Unmanned aerial vehicle meets vehicle-to-everything in secure communications," *IEEE Commun. Mag.*, vol. 57, no. 10, pp. 98–103, Oct. 2019.

[3] L. Reichardt, J. Maurer, T. Fügen, and T. Zwick, "Virtual drive: A complete V2X communication and radar system simulator for optimization of multiple antenna systems," *Proc. IEEE*, vol. 99, no. 7, pp. 1295–1310, Jul. 2011.

[4] M. G. N. Alsath and M. Kanagasabai, "Compact UWB monopole antenna for automotive communications," *IEEE Trans. Antennas Propag.*, vol. 63, no. 9, pp. 4204–4208, Sep. 2015.

[5] N. Herscovici, C. Christodoulou, E. R. Iglesias, O. Q. Teruel, and M. S. Fernandez, "Compact multimode patch antennas for MIMO applications [Wireless Corner]," *IEEE Antennas Propag. Mag.*, vol. 50, no. 2, pp. 197–205, Apr. 2008.

[6] K. Zhang, Z. H. Jiang, W. Hong, and D. H. Werner, "A low-profile and wideband triple-mode antenna for wireless body area network concurrent on-/off-body communications," *IEEE Trans. Antennas Propag.*, vol. 68, no. 3, pp. 1982–1994, Mar. 2020.

[7] W. S. Wang et al., "Compact quad-element vertically-polarized high-isolation wideband MIMO antenna for vehicular base station," *IEEE Trans. Veh. Techn.*, vol. 69, no. 9, pp. 10000–10008, Sep. 2020.

[8] D. Ribbenfjärd, B. Lindmark, B. Karlsson, and L. Eklund, "Omnidirectional vehicle antenna for measurement of radio coverage at 2 GHz v.2.0," *IEEE Antennas Wireless Propag. Lett.*, vol. 3, pp. 269–272, 2004.

[9] H. Wong, K. K. So, and X. Gao, "Bandwidth enhancement of a monopolar patch antenna with V-shaped slot for car-to-car and WLAN communications," *IEEE Trans. Veh. Technol.*, vol. 65, no. 3, pp. 1130–1136, Mar. 2016.

[10] N. N. Trong, S. P. Pinapati, D. Hall, A. Piotrowski, and C. Fumeaux, "Ultralow-profile and flush-mounted monopolar antennas integrated into a metallic cavity," *IEEE Antennas Wireless Propag. Lett.*, vol. 17, no. 1, pp. 86–89, Jan. 2018.

[11] J. Oh and K. Sarabandi, "Low profile vertically polarized omnidirectional wideband antenna with capacitively coupled parasitic elements," *IEEE Trans. Antennas Propag.*, vol. 62, no. 2, pp. 977–982, Feb. 2014.

[12] K. Sarabandi and M. Casciato, "Efficient calculation of the fields of a dipole radiating above an impedance surface," *IEEE Trans. Antennas Propag.*, vol. 50, no. 9, pp. 1222–1235, Sep. 2002.

[13] C. A. Balanis, *Antennas and Theory: Analysis and Design*, 3rd ed. New York, NY, USA: Harper & Row, 1982.

[14] Z. H. Jiang and W. Hong, "Design and experiments of bandwidth-controllable broadband monopole antennas with conformal anisotropic impedance surface coatings," *IEEE Trans. Antennas Propag.*, vol. 66, no. 3, pp. 1133–1142, Mar. 2018.

[15] Z. H. Jiang, M. D. Gregory, and D. H. Werner, "A broadband monopole antenna enabled by an ultrathin anisotropic metamaterial coating," *IEEE Antennas Wireless Propag. Lett.*, vol. 10, pp. 1543–1546, Dec. 2011.

[16] J. X. Liang, C. C. Chiau, X. D. Chen, and C. G. Parini, "Study of a printed circular disc monopole antenna for UWB applications," *IEEE Trans. Antennas Propag.*, vol. 53, no. 11, pp. 3500–3504, Nov. 2005.

[17] N. P. Agrawall, G. Kumar, and K. P. Ray, "Wide-band planar monopole antennas," *IEEE Trans. Antennas Propag.*, vol. 46, no. 2, pp. 294–295, Feb. 1998.

[18] S. Y. Suh, W. L. Stutzman, and W. A. Davis, "A new ultrawideband printed monopole antenna: The planar inverted cone antenna (PICA)," *IEEE Trans. Antennas Propag.*, vol. 52, no. 5, pp. 1361–1394, May 2004.

[19] W. B. Hong and K. Sarabandi, "Low profile miniaturized planar antenna with omnidirectional vertically polarized radiation," *IEEE Trans. Antennas Propag.*, vol. 56, no. 6, pp. 1533–1540, Jun. 2008.

[20] A. Al-Zoubi, F. Yang, and A. Kishk, "A broadband center-fed circular patch-ring antenna with a monopole like radiation pattern," *IEEE Trans. Antennas Propag.*, vol. 57, no. 3, pp. 789–792, Mar. 2009.

[21] J. Liu, Q. Xue, H. Wong, H. W. Lai, and Y. Long, "Design and analysis of a low-profile and broadband microstrip monopolar patch antenna," *IEEE Trans. Antennas Propag.*, vol. 61, no. 1, pp. 11–18, Jan. 2013.

[22] K. Zhang, Z. H. Jiang, T. Yue, Y. Zhang, W. Hong, and D. H. Werner, "A compact dual-band triple-mode antenna with pattern and polarization diversities enabled by shielded mushroom structures," *IEEE Trans. Antennas Propag.*, vol. 69, no. 10, pp. 6229–6243, Oct. 2021.

[23] S. Yan and G. A. E. Vandenbosch, "Low-profile dual-band pattern diversity patch antenna based on composite right/left-handed transmission line," *IEEE Trans. Antennas Propag.*, vol. 65, no. 6, pp. 2808–2815, Jun. 2017.

[24] J. D. Lin, Z. P. Qian, W. Q. Cao, S. J. Shi, Q. Q. Wang, and W. Zhong, "A low-profile dual-band dual-mode and dual-polarized antenna based on AMC," *IEEE Antennas Wireless Propag. Lett.*, vol. 16, pp. 2473–2476, 2017.

[25] H. Nakano, H. Iwaoka, K. Morishita, and J. Yamauchi, "A wideband low-profile antenna composed of a conducting body of revolution and a shorted parasitic ring," *IEEE Trans. Antennas Propag.*, vol. 56, no. 4, pp. 1187–1192, Apr. 2008.
[26] A. A. Omar and Z. X. Shen, "A compact and wideband vertically polarized monopole antenna," *IEEE Trans. Antennas Propag.*, vol. 67, no. 1, pp. 626–631, Jan. 2019.
[27] M. Koohestani, J.-F. Zürcher, A. A. Moreira, and A. K. Skrivervik, "A novel, low-profile, vertically-polarized UWB antenna for WBAN," *IEEE Trans. Antennas Propag.*, vol. 62, no. 4, pp. 1888–1894, Apr. 2014.
[28] A. Elsherbini and K. Sarabandi, "Very low-profile top-loaded UWB coupled sectorial loops antenna," *IEEE Antennas Wireless Propag. Lett.*, vol. 10, pp. 800–803, 2011.
[29] S. C. Wen and Y. D. Dong, "A low-profile wideband antenna with monopolelike radiation characteristics for 4G/5G indoor micro base station application," *IEEE Antennas Wireless Propag. Lett.*, vol. 19, no. 12, pp. 2305–2309, Dec. 2020.
[30] W. S. Wang et al., "Compact quad-element vertically-polarized high-isolation wideband MIMO antenna for vehicular base station," *IEEE Trans. Veh. Technol.*, vol. 69, no. 9, pp. 10000–10008, Sep. 2020.
[31] E. Yetisir, C. C. Chen, and J. L. Volakis, "Wideband low profile multiport antenna with omnidirectional pattern and high isolation," *IEEE Trans. Antennas Propag.*, vol. 64, no. 9, pp. 3777–3786, Sep. 2016.
[32] J.- K. Che, C. C. Chen, and J. F. Locke, "A compact four-channel MIMO 5G sub-6 GHz/LTE/WLAN/V2X antenna design for modern vehicles," *IEEE Trans. Antennas Propag.*, vol. 69, no. 11, pp. 7290–7297, Nov. 2021.
[33] M. A. Elmansouri and D. S. Filipovic, "Miniaturization of TEM horn using spherical modes engineering," *IEEE Trans. Antennas Propag.*, vol. 64, no. 2, pp. 5064–5073, Dec. 2016.
[34] M. A. Elmansouri, J. Ha, and D. S. Filipovic, "Ultrawideband TEM horn circular array," *IEEE Trans. Antennas Propag.*, vol. 65, no. 3, pp. 1374–1379, Mar. 2017.
[35] A. Alipour and H. R. Hassani, "A novel omni-directional UWB monopole antenna," *IEEE Trans. Antennas Propag.*, vol. 56, no. 12, pp. 3854–3857, Dec. 2008.
[36] J.- K. Che, C.-C. Chen, and J. F. Locke, "A compact cavity-backed tri-band antenna design for flush mount GNSS (L1/L5) and SDARS operations," *IEEE Antennas Wireless Propag. Lett.*, vol. 20, no. 5, pp. 638–642, May 2011.
[37] D. S. Filipovic and J. L. Volakis, "A flush-mounted multifunctional slot aperture (combo-antenna) for automotive applications," *IEEE Trans. Antennas Propag.*, vol. 52, no. 2, pp. 563–571, Feb. 2004.
[38] A. Chen, T. Jiang, Z. Chen, D. Su, W. Wei, and Y. Zhang, "A wideband VHF/UHF discone-based antenna," *IEEE Antennas Wireless Propag. Lett.*, vol. 10, pp. 450–453, 2011.
[39] E. G. Tianang, M. A. Elmansouri, and D. S. Filipovic, "Ultrawideband flush-mountable dual-polarized vivaldi antenna," *IEEE Trans. Antennas Propag.*, vol. 68, no. 7, pp. 5670–5674, Jul. 2020.
[40] M. A. Elmansouri and D. S. Filipovic, "Ultrawideband flush-mounted antenna," *IEEE Antennas Wireless Propag. Lett.*, vol. 16, pp. 1973–1976, 2017.
[41] D.-H. Kwon, "Transformation electromagnetic design of an embedded monopole in a ground recess for conformal applications," *IEEE Antennas Wireless Propag. Lett.*, vol. 9, pp. 432–435, 2010.
[42] C. D. Emiroglu and D. H. Kwon, "Design and realization of virtual line source using metamaterials," *IEEE Trans. Antennas Propag.*, vol. 64, no. 12, pp. 5220–5229, Dec. 2016.
[43] L. Z. Zheng and D. N. C. Tse, "Diversity and multiplexing: A fundamental tradeoff in multiple-antenna channels," *IEEE Trans. Inf. Theory*, vol. 49, no. 5, pp. 1073–1096, May 2003.
[44] C. Waldschmidt and W. Wiesbeck, "Compact wide-band multimode antennas for MIMO and diversity," *IEEE Trans. Antennas Propag.*, vol. 52, no. 8, pp. 1962–1969, Aug. 2004.
[45] Y. Zhang, W. Hong, C. Yu, Z. Q. Kuai, Y. D. Don, and J. Y. Zhou, "Planar ultrawideband antennas with multiple notched bands based on etched slots on the patch and/or split ring resonators on the feed line," *IEEE Trans. Antennas Propag.*, vol. 56, no. 9, pp. 3063–3068, Sep. 2008.
[46] Q. X. Chu and Y. Y. Yang, "A compact ultrawideband antenna with 3.4/5.5 GHz dual band-notched characteristics," *IEEE Trans. Antennas Propag.*, vol. 56, no. 12, pp. 3637–3644, Dec. 2008.
[47] J. Qiu, Z. Du, J. Lu, and K. Gong, "A planar monopole antenna design with band-notched characteristic," *IEEE Trans. Antennas Propag.*, vol. 54, no. 1, pp. 288–292, Jan. 2006.
[48] D. Z. Kim, W. I. Son, W.-G. Lim, H. L. Lee, and J. W. Yu, "Integrated planar monopole antenna with microstrip resonators having band-notched characteristics," *IEEE Trans. Antennas Propag.*, vol. 58, no. 9, pp. 2837–2842, Sep. 2010.
[49] Y. Cui, Y. Niu, Y. Qin, and R. Li, "A new high-isolation broadband flush-mountable dual-polarized antenna," *IEEE Trans. Antennas Propag.*, vol. 66, no. 12, pp. 7342–7347, Dec. 2018.
[50] R. G. Vaughan and J. B. Andersen, "Antenna diversity in mobile communications," *IEEE Trans. Veh. Technol.*, vol. VT-36, no. 4, pp. 149–172, Nov. 1987.
[51] Z. H. Jiang et al., "A compact triple-band antenna with a notched ultra-wideband and its MIMO array," *IEEE Trans. Antennas Propag.*, vol. 66, no. 12, pp. 7021–7031, Dec. 2018.
[52] S. Blanch, J. Romeu, and I. Corbella, "Exact representation of antenna system diversity performance from input parameter description," *Electron. Lett.*, vol. 39, no. 9, pp. 705–707, May 2003.

KE ZHANG (Student Member, IEEE) was born in Changzhou, Jiangsu, China, in 1993. He received the B.S. degree from the Suzhou University of Science and Technology in 2015, and the M.S. degree from the School of Electronic Information, Soochow University, Suzhou, China, in 2018. He is currently pursuing the Ph.D. degree with Southeast University, Nanjing, China.

His main research includes antennas, circuits, systems for microwave, and millimeter-wave wireless communications.

Mr. Zhang was a recipient of the 2017 and 2021 National Scholarship for Master and Doctoral Students. He received the Best Student Paper Award at the 2019 Asia-Pacific Conference on Antennas and Propagation held in Incheon, South Korea, the 2021 National Conference on Microwave and Millimeter Wave held in Nanjing, China, and the 2021 National Conference on Antennas held in Ningbo, China. He serves as a Reviewer for IEEE TRANSACTIONS ON ANTENNAS AND PROPAGATION.

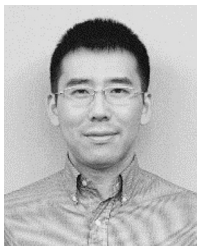

ZHI HAO JIANG (Member, IEEE) was born in Nanjing, China, in 1986. He received the B.S. degree in radio engineering from Southeast University, Nanjing, in 2008, and the Ph.D. degree in electrical engineering from The Pennsylvania State University, University Park, State College, PA, USA, in 2013.

From 2013 to 2016, he was a Postdoctoral Fellow with the Computational Electromagnetics and Antennas Research Laboratory, Department of Electrical Engineering, The Pennsylvania State University. He is currently a Professor with the State Key Laboratory of Millimeter Waves, School of Information Science and Engineering, Southeast University. He has also co-edited two books: *Electromagnetic Vortices: Wave Phenomena and Engineering Applications* (Wiley/IEEE Press, 2021) and *Electromagnetics of Body-Area Networks: Antennas, Propagation, and RF Systems* (Wiley/IEEE Press, 2016). He has authored or coauthored more than 100 papers in peer-reviewed journals, over 80 papers in conference proceedings, as well as 9 book chapters. He holds 7 granted U.S. patents and 18 granted Chinese patents. His current research interests include microwave/millimeter-wave antennas and circuits, millimeter-wave systems, impedance surfaces, metamaterials, and analytical methods. He was a recipient of the 2012 A. J. Ferraro Outstanding Doctoral Research Award in Electromagnetics, the Thousands of Young Talents presented by China Government in 2016, the High-Level Innovative and Entrepreneurial Talent presented by Jiangsu Province, China, in 2017, the Young Scientist Award at the 2019 ACES-China Conference, the Young Scientist Award at the URSI-GASS in 2020, the IEEE Microwave Prize in 2021, the Outstanding Youth Scholar of National Science Foundation of China in 2021, the ZTE Outstanding Collaboration Program Award in 2022, and Several Best (Student) Paper Awards at International Conferences. He serves as an Associate Editor of *IET Communications*. He is serving as a Committee Member of the IEEE AP-S New Technology Direction Committee and has served as the TPC Co-Chair or a TPC Member for multiple international conferences. He was a Guest Editor of *International Journal of RF and Microwave Computer-Aided Engineering*. He is a Senior Member of CIE

WEN LONG ZHOU was born in Taizhou, China, in 1988. He received the B.S. degree in electrical engineering from Xidian University, Xi'an, in 2010, and the M.S. degree in electrical engineering from Nanjing University, Nanjing, in 2016.

He worked as a RF Engineer with CommScope and Larid Technologies for several years. Since 2019, he has been serving as a RF System Engineer with Ford Motor Company. His main research includes antenna researches and developments in automotive, navigation systems, and base station applications.

PENG PENG was born in 1986. He received the B.S. and M.S. degrees from Southeast university, Nanjing, in 2007 and 2010, respectively. He worked as an EMC and an Antenna Engineer with Ford Motor Research and Engineering Center, Nanjing, China.

WEI HONG (Fellow, IEEE) received the B.S. degree in radio engineering from the University of Information Engineering, Zhengzhou, China, in 1982, and the M.S. and Ph.D. degrees in radio engineering from Southeast University, Nanjing, China, in 1985 and 1988, respectively.

He has been with the State Key Laboratory of Millimeter Waves, Southeast University, since 1988, where he has also been the Director of the Laboratory since 2003. He is currently a Professor of the School of Information Science and Engineering with Southeast University. He was a Short-Term Visiting Scholar with the University of California at Berkeley in 1993, and a Short-Term Visiting Scholar with the University of California at Santa Cruz, Santa Cruz, CA, USA, from 1995 to 1998. He has authored or coauthored over 300 technical publications and authored two books. His current research interests include numerical methods for electromagnetic problems, millimeter-wave theory and technology, antennas, electromagnetic scattering, and RF technology for mobile communications. He twice awarded the National Natural Prizes and thrice awarded the First-Class Science and Technology Progress Prizes issued by the Ministry of Education of China and Jiangsu Province Government. Besides, he also received the Foundations for China Distinguished Young Investigators and for "Innovation Group" issued by the NSF of China. He is the Vice President of the CIE Microwave Society and Antenna Society and the Chair of the IEEE MTTS/APS/EMCS Joint Nanjing Chapter. He served as an Associate Editor for the IEEE TRANSACTIONS ON MICROWAVE THEORY AND TECHNIQUES from 2007 to 2010, and one of the Guest Editors for the 5G special issue of the IEEE Transactions on Antennas and Propagation in 2017. He was an Elected IEEE MTT-S AdCom Member from 2014 to 2016. He is a Fellow of IEEE and CIE.